



HAL
open science

A dialogue between different approaches to fracture for predicting a crack nucleation at the microscale

Sara Jiménez-Alfaro, Dominique Leguillon, Corrado Maurini, José Reinoso

► To cite this version:

Sara Jiménez-Alfaro, Dominique Leguillon, Corrado Maurini, José Reinoso. A dialogue between different approaches to fracture for predicting a crack nucleation at the microscale. *International Journal of Fracture*, 2024. hal-04622643

HAL Id: hal-04622643

<https://hal.science/hal-04622643>

Submitted on 24 Jun 2024

HAL is a multi-disciplinary open access archive for the deposit and dissemination of scientific research documents, whether they are published or not. The documents may come from teaching and research institutions in France or abroad, or from public or private research centers.

L'archive ouverte pluridisciplinaire **HAL**, est destinée au dépôt et à la diffusion de documents scientifiques de niveau recherche, publiés ou non, émanant des établissements d'enseignement et de recherche français ou étrangers, des laboratoires publics ou privés.

A dialogue between different approaches to fracture for predicting a crack nucleation at the microscale

Sara Jiménez-Alfaro^{1,2*}, Dominique Leguillon³, Corrado Maurini³,
José Reinoso^{4,5,6}

^{1*}Department of Civil and Environmental Engineering, Imperial College London, Exhibition Road, London, SW7 2AZ, United Kingdom.

²Department of Engineering Science, University of Oxford, Parks Road, Oxford, OX1 3PJ, United Kingdom.

³Institut Jean Le Rond d'Alembert, Sorbonne Université, 4, Place Jussieu, Paris, 75005, France.

⁴Departamento de Mecánica de Medios Continuos y Teoría de Estructuras, ETS Ingeniería, Universidad de Sevilla, Camino de los Descubrimientos S/N, 41092 Seville, Spain.

⁵Grupo de Ingeniería de Estructuras y Materiales. Escuela Politécnica Superior, Universidad de Sevilla, C/ Virgen de África, 7, Sevilla, 41011, Spain.

⁶ ENGREEN - Laboratory of Engineering for Energy and Environmental Sustainability, Universidad de Sevilla, Seville, Spain.

*Corresponding author(s). E-mail(s): s.jimenez-alfaro@imperial.ac.uk;
sara.jimenezalfaro@eng.ox.ac.uk;

Abstract

Unraveling the material behavior at the microscale is one of the challenges of this century, demanding progress in experimental and computational strategies. Among the latter, two approaches are commonly applied for predicting crack nucleation. The Coupled Criterion (CC) and the Phase Field (PF) model, both depending on a material length parameter. In brittle materials at the macroscale, this parameter is significantly smaller than the specimen size. However, when the scale decreases, this material length might approach the structural dimensions. In this context, a comprehensive comparison between the two models is conducted,

changing the ratio between the material length parameter and the dimensions of the specimen. Results indicate that when this ratio is sufficiently small predictions from both models coincide, otherwise both the CC and the PF model predict different results. Despite their differences, a good agreement with experiments reported in the literature have been observed.

Keywords: Phase Field, Coupled Criterion, Microscale, Brittle fracture

1 Introduction

The latest advancements in microscopy have revealed that the microstructure of materials is crucial for enhancing their properties at the microscale, thus setting the stage for the development of new materials of high technological impact. Consequently, unraveling the material behavior at the microscale has emerged as a primary objective in this century. One of the most interesting properties to prevent nucleation or propagation of cracks is the brittleness of materials such as ceramics, where this inherent characteristic limits their application, despite numerous advantages, such as thermal properties or high resistance to oxidation or corrosion [1]. The emergence of advanced ceramics like alumina zirconia, has demonstrated the potential to enhance the brittleness of traditional ceramics. However, the full development of this new technology requires a comprehensive understanding of fracture behavior at lower scales. While a wide range of experimental techniques have been introduced, such as the nano-indentation [2] or the Micro-Electro-Mechanical System (MEMS) [3], it is equally critical to evaluate the suitability of applying numerical methodologies typically used at the macroscale to predict crack initiation and propagation at the microscale. Among these methodologies two prominent models within the context of Fracture Mechanics stand out: the Coupled Criterion (CC)[4, 5], within the framework of Finite Fracture Mechanics (FFM), and the gradient damage model for brittle fracture [6, 7], frequently named as a Phase Field (PF) model for brittle fracture [8].

One of the fundamental ingredients of FFM is the assumption that a crack jumps a finite length upon nucleation. This can be formulated through the CC [4], obtaining that this length depends on the material toughness, the tensile strength and the geometry. In contrast, the gradient damage model for brittle fracture presented in [6] introduces a material-related length that describes the size of the damaged region, called the phase field length scale. Both the PF length scale and the nucleation length obtained by the CC are proportional to the Irwin length defined by material properties. At the macro-scale, they are relatively small compared to structural dimensions, whereas at the micro-scale they become comparable or even larger, and can interact with the dimensions of the structure. In this context, the main objective of this paper is to investigate the applicability of both the CC and the PF model when descending the scales, presenting a reflective comparison between the two methodologies and contrasting them with selected experiments found in the literature.

On the one hand, the applicability of the CC at the microscale has been investigated in previous works. In 2020, Doitrand et al. [9] investigated the relationship between the

maximum flexural stress in a four-point bending test and the tensile strength across scales using the CC, while Gallo et al. [10] studied the FFM at the nanoscale, comparing results with experiments. In 2021, Jimenez-Alfaro and Leguillon [11] investigated the application of the CC across scales in ceramic materials, employing case studies and comparing results to experiments found in the literature. Moreover, in 2023, Baldassari et al. [12] applied the FFM approach to investigate the size effect of quasi-brittle materials, in particular, concrete and rock samples, obtaining a good agreement with experimental results.

On the other hand, one of the initial works regarding the applicability of the PF model when descending the scales is the one of Tanne et al. in 2018 [13], where they studied the crack nucleation in various geometries and the effect of a defect size with respect to the phase field length scale. Moreover, an important investigation related to composites has been developed in the last years, since the micromechanical analysis is essential to define the fracture behaviour of these materials at the mesoscale. In particular, in 2019 Guillen-Hernandez et al. [14] showed the applicability of the PF together with the Cohesive Zone Model (CZM) to predict failure initiation at the micro-scale, comparing with experiments and FFM predictions. Furthermore, Fantoni et al. [15] studied the influence of the micro-scale over the macro-scale results considering the PF model in composite materials. In 2020, Guillen-Hernandez et al. [16] investigated the in-situ effect found in transverse matrix cracking phenomena considering the PF model. Finally, in 2023 Macias et al. [17] provided a guidance to the application of the PF model for computational micro-mechanical studies in composite materials under 2D plane strain assumption.

Additional research has focused on the effect of the Fracture Process Zone (FPZ) in the fracture properties at the microscale [18], and the applicability of Linear Elastic Fracture Mechanics (LEFM) when the FPZ becomes significant [19]. Additionally, in 2020 Molnar et al. [20] included the effect of the process zone on the definition of the PF length scale, and the results were compared with those obtained by CC. This work was also explored in 2023 by Doitrand et al. [21], proposing a length free PF model, which was compared the CC results. An investigation of this approximation for daughter crack formation in antiplane shear is shown in [22] in 2024, including a comparison to the results obtained by the CC. Despite the extensive literature, none of these works have compared the CC and the PF model when descending the scales in homogeneous brittle materials, determining the influence of the relationship between the Irwin length and the dimensions of the specimen in the predictions.

The paper is structured as follows. Section 2 introduces the Coupled Criterion and the Phase Field model applied in this work. Section 3 analyzes the scale effect in various case studies, comparing the results obtained from both models. Section 4 compares the models with some experiments found in the literature. Finally, Section 5 presents the main conclusions drawn from this study.

2 Two different approaches to brittle fracture

The representation of fracture in brittle materials involves modeling the initiation and propagation of cracks, which can be achieved through two distinct approaches: discrete

and continuous models. In discrete models, such as the renowned Griffith model [23] or the Coupled Criterion [5], the crack is treated as a discontinuity in the material. Conversely, continuous models conceptualize cracks as damaged zones with reduced stiffness [24].

2.1 The Coupled Criterion

First, the Coupled Criterion relies on two conditions: an energy condition and a stress condition [4]. The energy condition is based on an energy balance encompassing two states of the loaded structure: one prior (0) and the other following (1) the initiation of a crack,

$$\Pi_p^{(0)} + \Pi_k^{(0)} = \Pi_p^{(1)} + \Pi_k^{(1)} + G_c \delta S. \quad (1)$$

Assuming a zero kinetic energy before the crack onset, $\delta \Pi_k \geq 0$, and therefore

$$\delta \Pi_p^{(0)} + G_c \delta S \leq 0. \quad (2)$$

In a 2D domain the energy balance is referred to the admissible crack extension δl ,

$$\delta \Pi_p^{(0)} + G_c \delta l \leq 0. \quad (3)$$

which is simplified introducing the Incremental Energy Release Rate (IERR) [4], named as G_{inc} ,

$$G_{\text{inc}} = -\frac{\delta \Pi_p}{\delta l} \geq G_c. \quad (4)$$

In the stress condition the tensile stress along the expected crack path is compared with the tensile strength (non-local condition),

$$\sigma(s) \geq \sigma_c \quad \text{for} \quad 0 \leq s \leq \delta l, \quad (5)$$

where s is the coordinate along the expected crack path. To sum up, the Coupled Criterion is based on two conditions

$$\bar{G}_{\text{inc}} = \frac{G_{\text{inc}}(\delta l)}{G_c} \geq 1, \quad (6)$$

$$\bar{\sigma} = \frac{\sigma(s)}{\sigma_c} \geq 1, \quad \text{for} \quad 0 \leq s \leq \delta l, \quad (7)$$

Two approaches can be used when applying the CC: The Matched Asymptotics (MA) and the Full Finite Element (FFE) approach. In this paper, the FFE one is used, since the nucleation length can be of the order of the dimensions of the specimen at the microscale [11].

2.2 The Phase Field model

Discrete models such as the one previously presented face limitations in situations where the crack path is not known a priori. In those situations, continuous models have

a significant advantage, although discrete models such as the one previously presented are typically simpler. One type of continuous model is the gradient damage model [6, 7], where a damage variable α is used to define stiffness degradation. Typically $0 \leq \alpha \leq 1$, where $\alpha = 1$ and $\alpha = 0$ represents the damaged and undamaged states respectively. Assuming a solid Ω loaded by a time-dependent body force \underline{b} and a contour force \underline{t} on $\partial_t\Omega$, the following total energy functional $\Psi_{l_{\text{pf}}}$ is defined,

$$\Psi_{l_{\text{pf}}}(\underline{u}, \alpha) = \int_{\Omega} \psi_{l_{\text{pf}}}(\underline{\underline{\varepsilon}}(\underline{u}), \alpha, \nabla\alpha) dx - \int_{\Omega} \underline{b} \cdot \underline{u} dx - \int_{\partial_t\Omega} \underline{t} \cdot \underline{u} ds, \quad (8)$$

where the admissible displacement field \underline{u} and damage variable α are defined in the functional spaces

$$V_u := \underline{u} \in H^1(\Omega) : \underline{u} = \bar{u} \quad \text{on} \quad \partial_u\Omega, \quad (9)$$

$$V_\alpha := \alpha \in H^1(\Omega) : \alpha = \bar{\alpha} \quad \text{on} \quad \partial_\alpha\Omega. \quad (10)$$

In (8) the energy density $\psi_{l_{\text{pf}}}(\underline{\underline{\varepsilon}}(\underline{u}), \alpha, \nabla\alpha)$ is

$$\psi_{l_{\text{pf}}}(\underline{\underline{\varepsilon}}(\underline{u}), \alpha, \nabla\alpha) = \psi_{el}(\alpha, \underline{\underline{\varepsilon}}(\underline{u})) + \frac{G_c}{l_{\text{pf}}c_w} (w(\alpha) + l_{\text{pf}}^2 \|\nabla\alpha\|^2) \quad (11)$$

where the elastic energy density $\psi_{el}(\alpha, \underline{\underline{\varepsilon}}(\underline{u}))$ is split into two components $\psi_{el}^+(\alpha, \underline{\underline{\varepsilon}}(\underline{u}))$ and $\psi_{el}^-(\alpha, \underline{\underline{\varepsilon}}(\underline{u}))$, related to traction and compression strain components [25] respectively:

$$\psi_{el}(\alpha, \underline{\underline{\varepsilon}}(\underline{u})) = g(\alpha)\psi_{el}^+(\alpha, \underline{\underline{\varepsilon}}(\underline{u})) + \psi_{el}^-(\underline{\underline{\varepsilon}}(\underline{u})), \quad (12)$$

being $g(\alpha) = (1 - \alpha)^2$ the degradation function. In this work, the strain energy split is based on the volumetric-deviatoric decomposition presented in [26].

$$\psi_{el}^+(\alpha, \underline{\underline{\varepsilon}}(\underline{u})) = \frac{K}{2} \langle \text{tr}(\underline{\underline{\varepsilon}}(\underline{u})) \rangle_+^2 + A_0 : \underline{\underline{\varepsilon}}_0(\underline{u}) : \underline{\underline{\varepsilon}}_0(\underline{u}), \quad (13)$$

$$\psi_{el}^-(\underline{\underline{\varepsilon}}(\underline{u})) = \frac{K}{2} \langle \text{tr}(\underline{\underline{\varepsilon}}(\underline{u})) \rangle_-^2, \quad (14)$$

where $\langle \text{tr}(\underline{\underline{\varepsilon}}) \rangle_{\pm} = \frac{\text{tr}(\underline{\underline{\varepsilon}}) \pm |\text{tr}(\underline{\underline{\varepsilon}})|}{2}$, K is the bulk modulus of the material and $\underline{\underline{\varepsilon}}_0(\underline{u})$ is the deviatoric part of the strain tensor.

In (11) a gradient term is introduced in the formulation to avoid spurious localization of damage in stress softening regimes [24]. This term depends on the gradient of the damage variable, introducing an internal length scale l_{pf} . The definition of l_{pf} is studied in [6, 27] based on a 1D analysis of a bar under tensile loading, where it is concluded that l_{pf} is a material property proportional to the Irwin length, defined as

$$l_{\text{Irwin}} = \frac{EG_c}{\sigma_c^2}. \quad (15)$$

The function $w(\alpha)$ in (11) fulfills that $w(0) = 0$ and $w(1) = 1$, and the coefficient $c_w := \int_0^1 \sqrt{w(s)} ds$. A first definition of $w(\alpha)$ and c_w is given when an elastic phase with no damage ($\alpha = 0$) is considered, after which there is a damaged phase where α evolves until the complete damage $\alpha = 1$ [6]. This model is known as the AT1 model, and

$$w(\alpha) = \alpha \quad \text{and} \quad c_w = 8/3. \quad (16)$$

If, on the contrary, no elastic phase is included, the following functions can be used

$$w(\alpha) = \alpha^2 \quad \text{and} \quad c_w = 1/2, \quad (17)$$

which is known as the AT2 model [27]. In these two models, the phase field length scale can be defined as a function of l_{Irwin} ,

$$l_{\text{pf}} = \frac{3}{8} l_{\text{Irwin}} \quad \text{for AT1}, \quad (18)$$

$$l_{\text{pf}} = \frac{27}{256} l_{\text{Irwin}} \quad \text{for AT2}. \quad (19)$$

The solution (\bar{u}, α) is described at each time $\tau > 0$ through the application of the evolution problem [6, 24]:

- **Irreversibility condition:** the damage variable must not decrease with time $\dot{\alpha} \geq 0$.
- **Stability condition:** At each time $\tau > 0$ the solution (\bar{u}, α) must be stable, i.e., there exists $\bar{h} > 0$ such that

$$\Psi_{l_{\text{pf}}}(\underline{u} + h(\hat{u} - \underline{u}), \alpha + h(\hat{\alpha} - \alpha)) \geq \Psi_{l_{\text{pf}}}(\underline{u}, \alpha), \quad (20)$$

for all $h \in [0, \bar{h}]$, $\hat{u} \in V_u$, $\hat{\alpha} \in V_\alpha$ and $\hat{\alpha} \geq \alpha$.

- **Energy balance:** at each time $\tau > 0$

$$\frac{\partial \Psi_{l_{\text{pf}}}(\underline{u}, \alpha)(0, \dot{\alpha})}{\partial \tau} \geq 0 \quad (21)$$

The gradient damage model presented above is inspired in the variational approach to brittle fracture introduced in [28], where a functional $\Psi(\Gamma, \underline{u})$ is minimized, depending on the crack surface Γ . Hence, based on Γ -convergence [29], it can be shown that the global minimizer of $\Psi_{l_{\text{pf}}}(\underline{u}, \alpha)$ would approach the global minimizer of $\Psi(\underline{u}, \Gamma)$ when $l_{\text{pf}} \rightarrow 0$ [30] in the absence of body and contour forces.

The numerical application of the PF model is achieved using the Finite Element Method (FEM). Two options can be formulated: monolithic or staggered schemes. The first ones are potentially more efficient, because the solution is obtained with only one iteration loop [8], although they need more time to be completed. On the contrary, the staggered schemes are more robust and for this reason they are the ones applied in this paper. For each time τ , an iterative process starts. First, the displacement field \underline{u}^i at iteration i is obtained while keeping constant the damage variable $\alpha^i = \alpha^{i-1}$. Then, the damage variable at iteration i denoted as α^i is calculated keeping constant \underline{u}^i . The process is iterated until the algorithm finds a convergence, based on $|\alpha^i - \alpha^{i-1}| < \text{Tol}$,

where Tol is a tolerance that must be adjusted in the problem. Note that the first iteration $i = 1$ uses the damage variable from the previous step. The software FEniCSx has been applied to develop the FEM codes in the CC and the PF model [31].

3 Case studies

In this section, several case studies are proposed to analyze how fracture behavior in materials changes when the ratio of the Irwin length divided by the specimen dimensions is varied, highlighting its effect at the microscale. Two models, the Coupled Criterion (CC) and the Phase Field (PF), are applied and compared in this analysis. The analysis begins with a preliminary remark in Section 3.1, the tensile test of a bar is presented. Subsequently, the study of an unnotched specimen in a bending test is examined in Section 3.2, followed by the bending test of a u-notched cantilever beam 3.3. Moreover, the source code used to solve the latter case is offered in the NewFrac repository¹.

3.1 A preliminary remark

In the context of this study, an elastic bar under tension, characterized by its length L and cross-sectional area S , is subjected to an applied tensile force F , as depicted in Fig. 1. The material composition of the bar is alumina zirconia, and its mechanical properties [32] are provided in Table 1. These properties are determined at the macroscale and it is assumed that they are not changed across scales, i.e., l_{Irwin} is considered the same in the whole analysis. The main objective of this analysis is to determine the parameter $\sigma_{\text{fail}}(L)$, defined as the maximum allowable tensile stress in the bar.

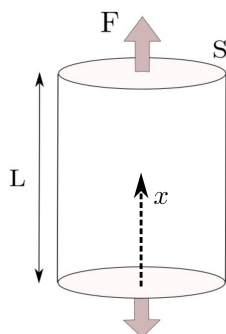


Fig. 1: Scheme of a bar in tension.

¹<https://zenodo.org/doi/10.5281/zenodo.11518790>

E [GPa]	ν	σ_c [MPa]	G_c [MPa mm]
380	0.22	400	0.023

Table 1: Mechanical properties of the alumina zirconia [32].

Application of the Coupled Criterion: The application of the CC predicts the crack nucleation when both the stress and the energy condition are satisfied. At the moment of failure, it is assumed that a sharp crack appears in the specimen, and the energy is abruptly reduced to zero. From the study conducted in [11] where this problem is analyzed, σ_{fail} is defined as

$$\sigma_{\text{fail}}(L) = \sigma_c \quad \text{if } L > 2l_{\text{Irwin}}, \quad (22)$$

$$\sigma_{\text{fail}}(L) = \sigma_c \sqrt{2 \frac{l_{\text{Irwin}}}{L}} \quad \text{if } L < 2l_{\text{Irwin}}. \quad (23)$$

where the characteristic Irwin length is defined in (15). It is observed that a critical length $2l_{\text{Irwin}}$ plays an important role in the crack nucleation. When $L > 2l_{\text{Irwin}}$, the failure stress is predominantly determined by the stress condition (7). In contrast, for cases where $L < 2l_{\text{Irwin}}$, the failure stress is primarily influenced by the energy condition (6), i.e., according to the CC, the size of the specimen is so small that it is necessary to increase the load in order to reach the failure. To illustrate this idea the evolution of σ_{fail} has been represented in Fig. 2, highlighting the region where either the stress or the energy condition is governing.

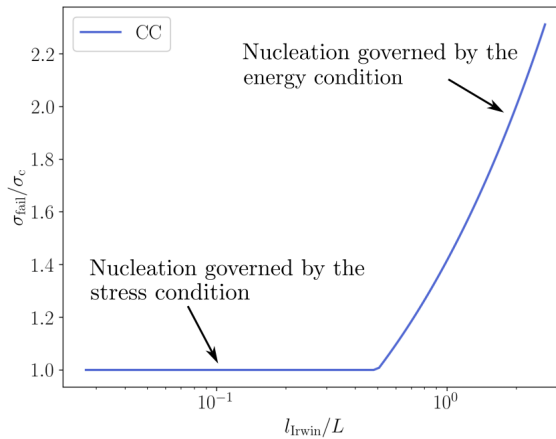


Fig. 2: Evolution of σ_{fail} with respect to l_{Irwin}/L of a homogeneous bar in tension, according to the CC.

Application of the Phase Field model: On the other hand, when applying the PF model two options can be explored if the boundary conditions of the damage

variable are changed [7]: BC1, which imposes no Dirichlet boundary conditions on α , and BC2, which enforces the condition $\alpha = 0$ at both ends of the bar. In BC1, the damage variable remains constant along the bar, allowing for the development of solutions with homogeneous damage. In BC2, a localized damaged region is observed, indicating that the crack breaks into two pieces after crack nucleation. In both cases σ_{fail} is defined in the same way as in the application of the CC, as the maximum allowable tensile stress in the structure. In the case of PF BC1, the solution yields $\sigma_{\text{fail}} = \sigma_c$. However, for PF BC2, the value of σ_{fail} depends on the ratio l_{Irwin}/L . For $L > l_{\text{Irwin}}$, the PF model defines a brittle failure of the structure. Therefore, when $\sigma = \sigma_{\text{fail}}$, a crack is abruptly nucleated across the beam and the solution shows a snap-back in the strain-stress response [33]. This case is illustrated in Fig. 3 where the evolution of $\sigma(\varepsilon)/\sigma_c$ is represented for $L = 10l_{\text{Irwin}}$. Moreover, in Fig. 4 the damage variable after failure is also shown, observing a narrow damage region representing the crack.

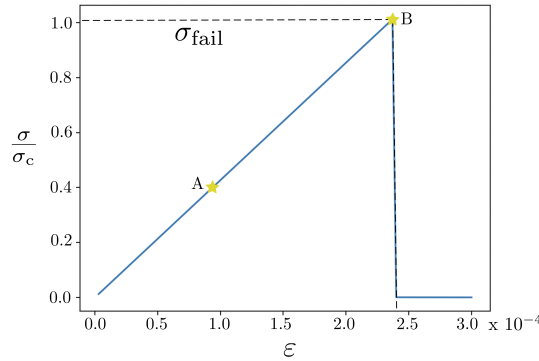


Fig. 3: Evolution of the tensile stress σ/σ_c with respect to the axial strain ε for the case BC2 and $L = 10l_{\text{Irwin}}$, according to the PF model. The failure stress σ_{fail} is highlighted. The points A, B correspond to damage fields in Fig. 7.

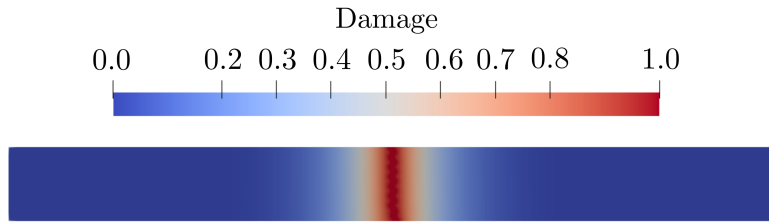


Fig. 4: Damage variable after failure for $L = 10l_{\text{Irwin}}$, according to the PF model in the BC2 case.

The PF model with BC2 conditions describes a different failure mode in the structure when $L < l_{\text{Irwin}}$. In that case, the current PF formulation does not predict a Griffith-like crack; instead, it predicts the development of a significant damage region, which generates the complete failure of the structure, as mentioned in [6]. Consequently, when $\sigma = \sigma_c$ a snap-back in the strain-stress response is not observed. Instead, an apparent strengthening effect is noticed, due to the extensive damage region, which amplifies the spread of damage, and therefore it is necessary to increase the load to reach failure. An example to illustrate this case is shown in Fig. 5 for $L = 3/8l_{\text{Irwin}}$, where the evolution of $\sigma(\varepsilon)/\sigma_c$ is represented. It can be observed that the highest value of $\sigma = \sigma_{\text{fail}}$ is bigger than σ_c . Furthermore, in Fig. 6 the damage variable after failure is also shown. A large damage region is now described by the PF model.

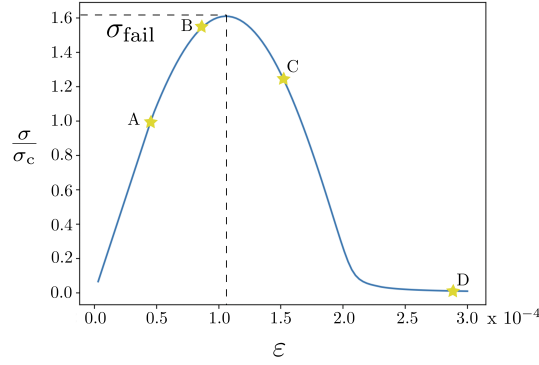


Fig. 5: Evolution of the tensile stress σ/σ_c with respect to the axial strain ε for the case BC2 and $L = 3/8l_{\text{Irwin}}$, according to the PF model. The failure stress σ_{fail} is highlighted. The points A, B, C, D correspond to damage fields in Fig. 7.

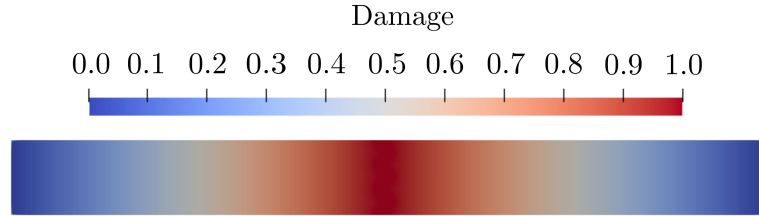


Fig. 6: Damage variable after failure for $L = 3/8l_{\text{Irwin}}$, according to the PF model in the BC2 case.

The evolution of the damage profile along the middle axis of the beam is represented in Fig. 7 for various loading scenarios in the two examples studied in Figs. 3 and 5.

For $L = 10l_{\text{Irwin}}$, the damage remains 0 until a critical loading point where $\sigma = \sigma_c$ and crack nucleation occurs. Therefore, only two profiles are observable, before and after fracture, the latter characterized by the point B in Fig. 3 and the second one by the point A (as an example). However, for $L = 3/8l_{\text{Irwin}}$, the damage profile progressively evolves until reaching a value of 1 (completely broken) in the bar, characterized by point D in Fig. 5. Damage begins to appear later than point A in Fig. 5, corresponding to $\sigma = \sigma_c$. Two intermediate loading points B and C in Fig. 5 are chosen to illustrate the progressive evolution of the damage region for $L = 3/8l_{\text{Irwin}}$. Furthermore, it is observed that the damaged area for $L = 3/8l_{\text{Irwin}}$ is much larger than the damaged area for $L = 10l_{\text{Irwin}}$ when the failure is fully developed (point B in Fig. 3 and point D in Fig. 5).

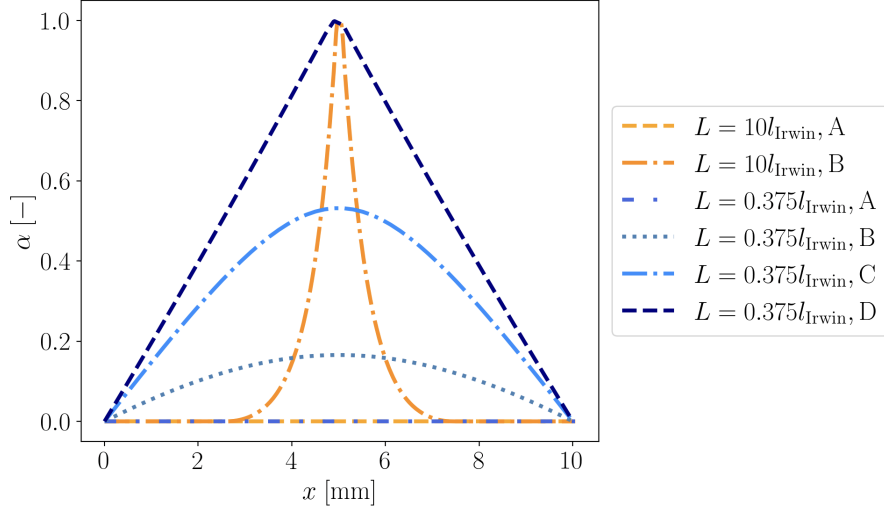


Fig. 7: Evolution of the damage variable α with respect to the axial direction x for different load cases highlighted in Figs. 4 and 5, for $L = 10l_{\text{Irwin}}$ and $L = 3/8l_{\text{Irwin}}$ respectively.

The three proposed evaluations of the failure stress (CC, PF BC1 and PF BC2) are represented in Fig. 8, where the selected range is $l_{\text{Irwin}}/L = 0.2 - 5$, considering that the minimum length of the bar is greater than the size of the FPZ estimated in [18]. An apparent strengthening effect is observed for both the CC and the PF BC2. Nevertheless, it is noticeable that this phenomenon differs significantly. This dissimilarity arises from their distinct inherent natures of both approaches. According to the CC, the failure of the structure is explained by the nucleation of a sharp crack, defined as a discontinuity in the material. The apparent strengthening is a consequence of the small size of the specimen, which has not enough energy to generate damage. However, according to the PF model, when the length of the specimen is less than l_{Irwin} , the failure is not generated by a sharp crack, it is explained by the development of a damage region where the stiffness is significantly and progressively reduced. The

size of the damage region is so big that the load is still increasing until the tensile stress is finally decreased, generating an apparent strengthening effect completely different to the one predicted by the CC.

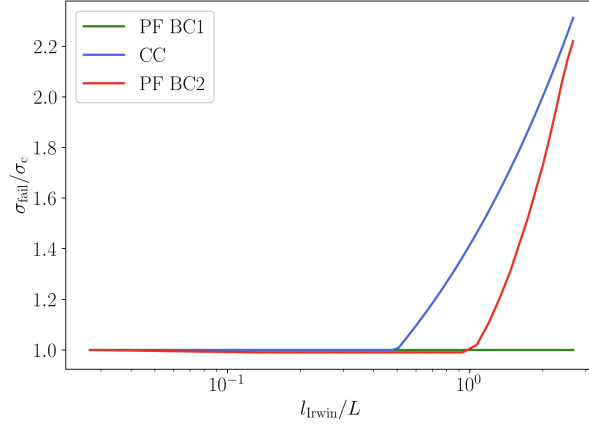


Fig. 8: Evolution of σ_{fail} with respect to l_{Irwin}/L of a homogeneous bar in tension, according to the CC and the PF model.

In conclusion, the response of the CC and the PF model varies depending on the relation between the Irwin length and the specimen dimensions, l_{Irwin}/L . When $l_{\text{Irwin}} \ll L$, both models predict the same response. However, when $l_{\text{Irwin}} \sim L$, the two models describe different scenarios, primarily because the PF model no longer predicts a brittle failure, unlike the CC model, which always defines the crack as a material discontinuity. As consequence, both models give different predictions when addressing scale-related effects, such as the apparent structural strengthening, highlighted in this section. However, both are able to show that the maximum allowable stress in the bar is a structural property instead of a material one when descending the scales. The upcoming sections aim to thoroughly investigate these differences and determine whether, despite them, both models can accurately approximate experiments involving situations where the control parameter l_{Irwin}/L is larger or of the order of 1.

3.2 Bending test of an unnotched specimen

In the study conducted in [11], the CC is applied to investigate the behaviour of an unnotched specimen in a 3-point bending test when the scale is changed (mm, μm ...) by varying G_c . In this paper, the study is conducted keeping constant G_c , to study the influence of the control parameter l_{Irwin}/W , where W is a characteristic dimension of the specimen.

The problem solved in [11], frequently encountered in the field of Solid Mechanics, is not a well-posed problem since it can lead to infinite energy in the vicinity of the point load. However, this challenge can effectively be addressed through the application of the CC, which defines the expected crack path a priori. This chosen crack path

is located at a considerable distance from the regions where the point loads are applied, preserving the validity of the elastic solution, justified under the Saint Venant's Principle. Nevertheless, the problem posed by point loads is not easily solved considering variational methods, since localized damage is observed in the vicinity of the region where the load is applied. One possible solution is to impose the Dirichlet boundary condition $\alpha = 0$ in these specific regions. This approach, however, would limit the crack growth, preventing it from attaining the width of the specimen. While this constraint has not difficulties for small values of σ_c , it complicates the convergence of the solution as σ_c increases, thereby increasing the damage energy within the solid. In cases where solution converges, a crack branching is predicted in the region where α can grow, which might deviate from reality. Hence, in this paper an alternative problem is introduced, involving the bending test of an unnotched specimen subjected to a distributed displacement applied at its ends, see Fig. 9 where $u(x_2)$ is defined as

$$u(x_2) = U \left(1 - \frac{x_2}{W} \right). \quad (24)$$

The specimen dimensions considered for the specimen are $L = 8 \mu\text{m}$ and $W = 1 \mu\text{m}$, with $E = 380 \text{ GPa}$ and $\nu = 0.22$, as the material properties. The tensile stress along the width of the specimen is also represented, where its maximum value is located in the lower part of the structure, and is named as flexural stress $\sigma_f = \sigma(s = 0)$. The main objective of the analysis is to determine the critical flexural stress σ_{fc} , defined as the maximum allowable σ_f reached in the structure, and the corresponding critical displacement U_c for which σ_{fc} is reached, as a function of the control parameter l_{Irwin}/W .

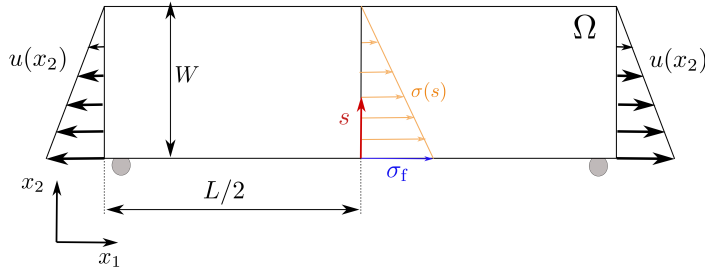


Fig. 9: Schematic view of an unnotched specimen in a bending test. The orange solid line is the tensile component of the stress tensor along the middle axis. In blue the flexural stress has been highlighted.

Application of the Coupled Criterion: One of the main difficulties when applying the CC in this problem is that although it is known that the crack grows through the specimen thickness, precisely defining its longitudinal position might not be possible, and therefore the expected crack path is unknown a priori. This situation is

easily solved when considering internal defects in the structure, since their presence is directly related to the position where the failure is localized, although this is beyond the scope of this analysis. In the context of the stress condition, this is not problematic, as the prescribed boundary conditions result in a constant tensile stress distribution along the longitudinal axis of the beam, see Fig. 10a where σ is represented for $U = 1$ at several axial positions in the solid (possible locations of the expected crack path). However, when considering the energy condition, G_{inc} is different depending on the longitudinal position where the crack is located, as it is illustrated in Fig. 10b for three longitudinal crack positions and $U = 1$.

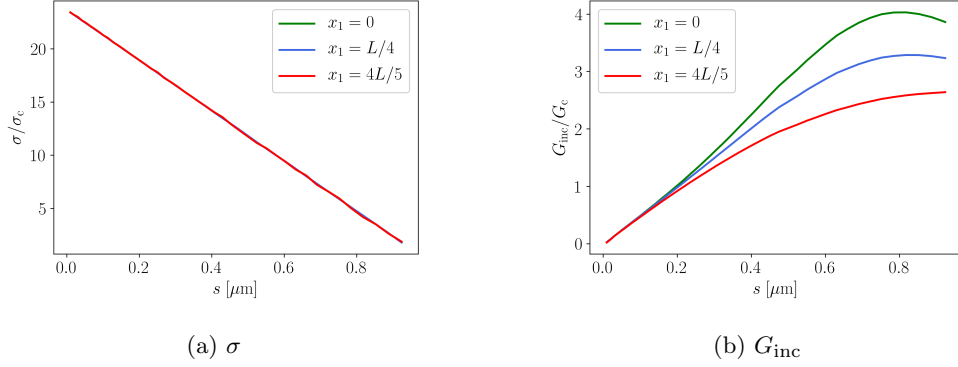


Fig. 10: Representation of the two main parameters used in the Coupled Criterion for three longitudinal positions of the expected crack path, considering $U = 1$.

Looking at Fig. 10b it can be observed that, for $s < 0.3 \mu\text{m}$, there is negligible disparity among the three curves. Consequently, the position of the crack along x_1 only assumes significance when the newly created crack length surpasses $0.3\mu\text{m}$, a scenario that is out of this study, since it is not observed in the chosen range of σ_c values, see Fig. 11, where the nucleation length obtained in the Coupled Criterion δl is represented as a function of l_{Irwin}/W (for the sake of simplicity δl has been calculated in the middle position as an example. To sum up, for the application of the CC in this context, the longitudinal position of the crack does not yield significance, and it does not introduce alterations to the values of U_c and σ_{fc} . Furthermore, it is observed in Fig. 11 that δl notably increases when the Irwin length is of the order of the dimensions of the specimen, a conclusion that was already observed in [11].

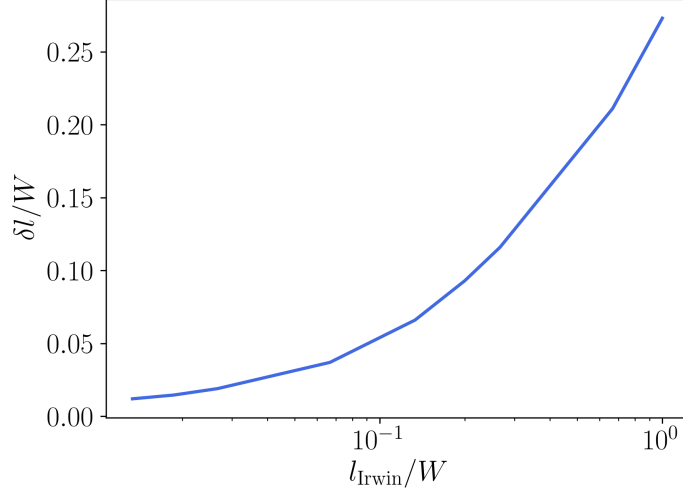


Fig. 11: Evolution of the nucleation length δl as a function of l_{Irwin}/W according to the CC.

Application of the Phase Field model: two options are available: either with no boundary conditions in the damage variable (BC1) or by applying the condition $\alpha = 0$ at both ends of the specimen (BC2). However, small differences have been observed between them in this case, and only the case BC1 is represented here. Hence, in Fig. 12 the function $\sigma_f(U)$ is represented for two different values of $l_{\text{Irwin}}/W = 0.001$ and 1, with BC1. In Fig. 12a, for $l_{\text{Irwin}}/W = 0.001$, a Griffith-like crack appears and σ_f starts decreasing when it reaches the tensile strength σ_c . However, when l_{Irwin}/W increases, as shown in Fig. 12b for $l_{\text{Irwin}}/W = 1$, the critical stress σ_{fc} is higher than σ_c , what is known as a structural strengthening effect. As was indicated in the Section 3.1, this phenomenon is observed because the damage variable does not abruptly change but evolves progressively. The damaged zone is no longer a small region in the material, and therefore there is no crack in the sense of Griffith.

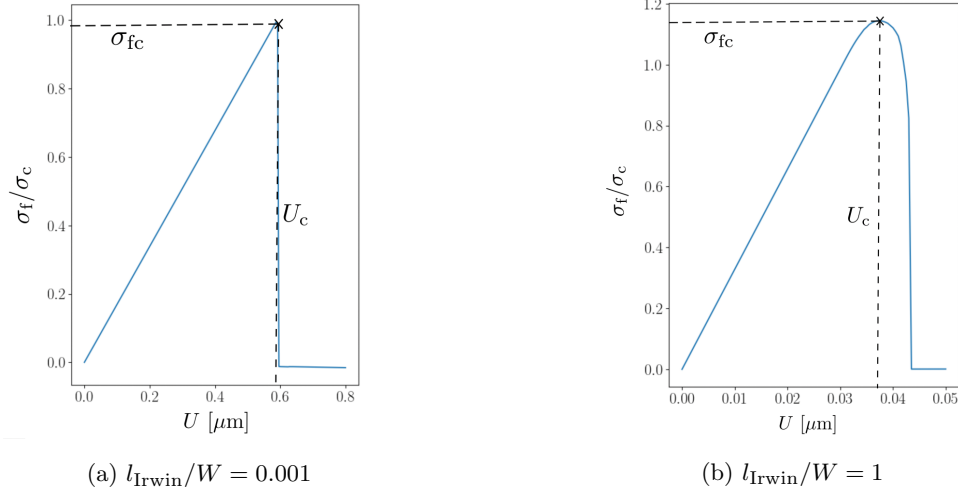


Fig. 12: Evolution of σ_f/σ_c with respect to U in the bending test of an unnotched specimen for two values of the control parameter $l_{\text{Irwin}}/W = 1$.

The critical flexural stress σ_{fc} and the corresponding critical displacement U_c obtained using both the CC method and the PF model are compared in Fig. 13. It is observed that both models predict a structural strengthening effect, see Fig. 13a, when the Irwin length reaches values comparable to the dimensions of the specimen. However, it is important to note that results obtained differ significantly between the two models. This disparity in predictions is primarily attributed to the capability of the phase field model to capture and consider diffuse damage dissipation, an aspect that is not accounted by the CC in any case. On the other hand, when the Irwin length is significantly smaller than the dimensions of the specimen, both models predict brittle fracture and the critical stress is equal to the tensile strength. In this scenario, the differences between the two models are minimized. It is relevant to note that, despite discrepancies in the stress solution between PF and CC, both models provide very similar estimations of U_c , as depicted in Fig. 13b. This phenomenon is due to the fact that the displacement range over which damage dissipation occurs in the PF model is relatively small and similar to the end of the elastic regime. Obviously, the evolution of the elastic regime in both models is identical, since the AT1 model is considered.

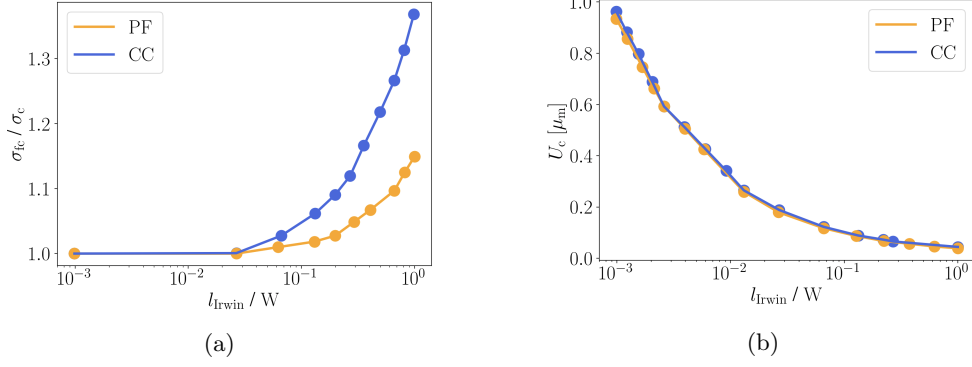


Fig. 13: Evolution of σ_{fc}/σ_c and U_c in the bending test of an unnotched specimen with respect to the control parameter l_{Irwin}/W .

3.3 Bending test of a u-notched cantilever beam

As mentioned in Section 1, bending tests of cantilever beams are extensively used to study fracture at the microscale. In this section, the application of the PF model is analyzed and compared to the use of the CC. The main objective is to investigate the impact of changing the control parameter $l_{\text{Irwin}}/(W-a)$, where $W-a$ is a characteristic dimension of the specimen, defined as the available width for the crack to grow, see Fig. 14. To that aim, an equivalent 2D plane strain model under displacement control is generated. This model is inspired by the experiments made in [34], where the fracture toughness and the critical force of a total of 14 specimens at the microscale are tested. In fact, reference dimensions in this section are taken from specimen number 6 in [34]: $L = 8.76 \mu\text{m}$, $W = 4.265 \mu\text{m}$, $n = 0.876 \mu\text{m}$, $a = 0.91 \mu\text{m}$ and $B = 4.42 \mu\text{m}$. Moreover, a blunt in the notch of $r = 0.01 \mu\text{m}$ is considered [11]. It is important to highlight that in Section 4.2, dedicated to experimental comparison, the 14 specimens are numerically tested and compared with results in [34], from the point of view of the PF model and the CC.

A previous study considering the CC is presented in [11]. In this paper, some modifications are included in the model, applying a distributed load instead of a point load to avoid the nucleation of local damage in the load application zone when applying the PF model, as it was done in Section 3.2. Hence, the main parameter studied is the critical force F_c , obtained using the critical distributed displacement u_c , as

$$F_c = \frac{2\Psi_{\text{el}}B}{u_c}, \quad (25)$$

where Ψ_{el} is the elastic energy stored in the equivalent 2D specimen, therefore it is multiplied by the thickness B to obtain the total force in the 3D problem.

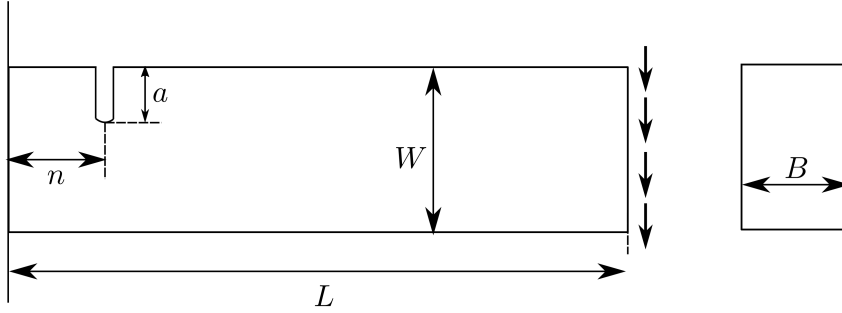


Fig. 14: Scheme of the equivalent 2D model used in this analysis, based on experiments in [35] and the model presented in [11].

One of the critical points in the numerical resolution of the problem presented in Fig. 14 is the choice of the mesh size h in the vicinity of the u-notch, where the crack nucleation is expected. In [36], it is defined that a size $h = l_{pf}/5$ is necessary to correctly capture the fracture process with the PF model. However, this magnitude competes in this problem with the notch blunt radius, which can be even smaller than l_{pf} . Consequently, when $r > 10l_{Irwin}$, $h = l_{pf}/5$ is taken; otherwise, $h = r/2$ to correctly capture the notch blunt in the discretized model.

Another important aspect in the model generation is the definition of Dirichlet boundary conditions on the damage variable. In [13], the idea of applying the condition $\alpha = 1$ on the faces of the notch is studied, distinguishing between the damaged and undamaged boundary conditions. The analysis conducted indicates that undamaged boundary conditions tend to overestimate the critical load, a similar conclusion to the one obtained in [37]. In this problem, three different options are studied. The first, NDBC, does not consider any damage boundary condition in the u-notch. The second, DBC1, considers the condition $\alpha = 1$ only in the u-notch blunt. The third, DBC2, considers the condition $\alpha = 1$ in the entire u-notch. Fig. 15 and 16 illustrate the three options for two cases, when $l_{pf} \ll (W - a)$ and $l_{pf} \approx (W - a)$.

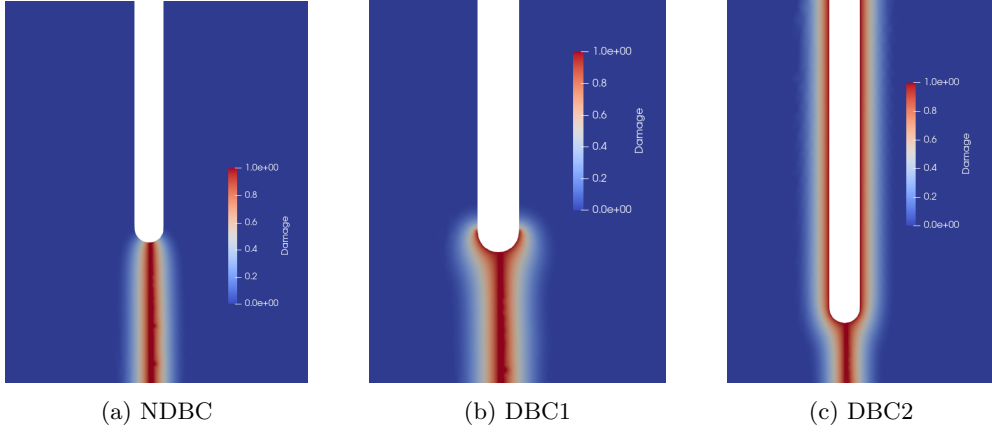


Fig. 15: Crack nucleation considering the three options for the damage boundary conditions for $l_{pf} \ll (W - a)$.

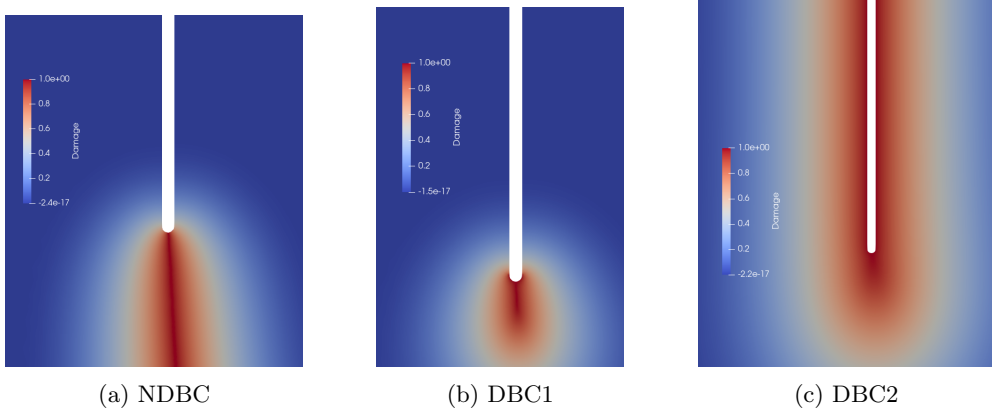


Fig. 16: Crack nucleation considering the three options for the damage boundary conditions for $l_{pf} \approx (W - a)$

Fig. 17 shows the critical force F_c as a function of σ_c for the three options, while keeping $K_c = 1.44 \text{ MPa m}^{0.5}$ constant, a value derived from experimental estimations for specimen 6 in [34]. It is observed that the NDBC option tends to overestimate the critical load, as previously indicated in [13]. The options DBC1 and DBC2 coincide for large values of σ_c , associated with small values of l_{Irwin} . However, as σ_c decreases and l_{Irwin} approaches the specimen dimensions, DBC1 and DBC2 diverge. This is because the size of the damaged region is proportional to l_{Irwin} according to the PF model studied in this paper. In the case of DBC2, when this value is significantly larger than

the specimen dimensions, the part of the notch that is not corresponding to the blunt radius has a greater contribution to damage diffusion, as indicated in Fig. 16. This is not the case for DBC1, where the damage is more localized. In the results presented below, the DBC1 option is chosen, although in Section 4.2 the NDBC and DBC1 are compared with experimental results. The DBC2 option is no longer studied, as it does not represent the physics of the problem for small values of σ_c .

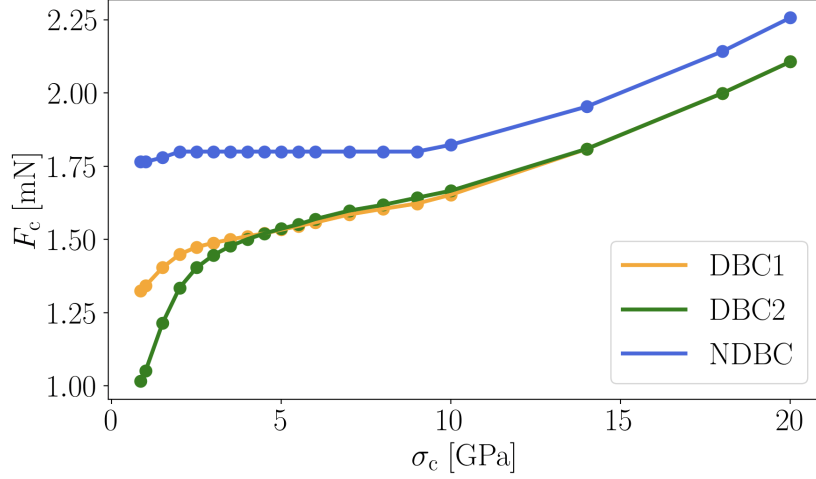


Fig. 17: Evolution of F_c as a function of σ_c for the three options in the damage boundary conditions: DBC1, DBC2 and NDBC.

In Fig. 17 the parameter F_c is calculated as the maximum allowable force in the structure. Since displacement control is considered in this analysis, this means that F_c is associated with a significant drop in the force - displacement curve. If force control were studied (as in Section 4.2), F_c would be related to a sudden and considerable increase in the displacement. This can be considered as a first criterion to define the failure in the structure and numerically estimate the critical force F_c , named here as FU. A second criterion, named as KU, defines the crack nucleation through a decrease in the structural stiffness. An example of these two criteria is illustrated in Fig. 18 for specimen 6 ($K_c^{\text{exp}} = 1.56 \text{ MPa m}^{0.5}$ and $\sigma_c^{\text{exp}} = 2500 \text{ MPa}$).

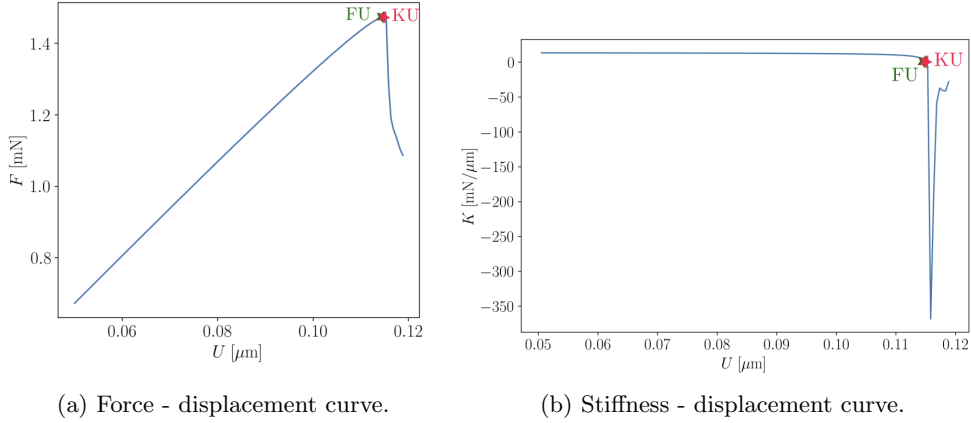


Fig. 18: Examples of a force-displacement and stiffness-displacement curve. These curves were obtained using the fracture properties and dimensions experimentally obtained in [34] for specimen 6 ($K_c^{\text{exp}} = 1.56 \text{ MPa m}^{0.5}$ and $\sigma_c^{\text{exp}} = 2500 \text{ MPa}$).

A third criterion, named as αU , involves understanding that crack nucleation occurs when the condition $\alpha = 1$ is reached at the notch tip. An example is illustrated in Fig. 19. In this case, the DBC2 conditions are considered, and crack nucleation is deemed to have occurred when the damage variable reaches $\alpha = 1$ at a node not initially affected by the damage boundary condition. This is represented through an damage-displacement diagram. In the case of force control, applied in Section 4.2, the damage-force diagram is considered.

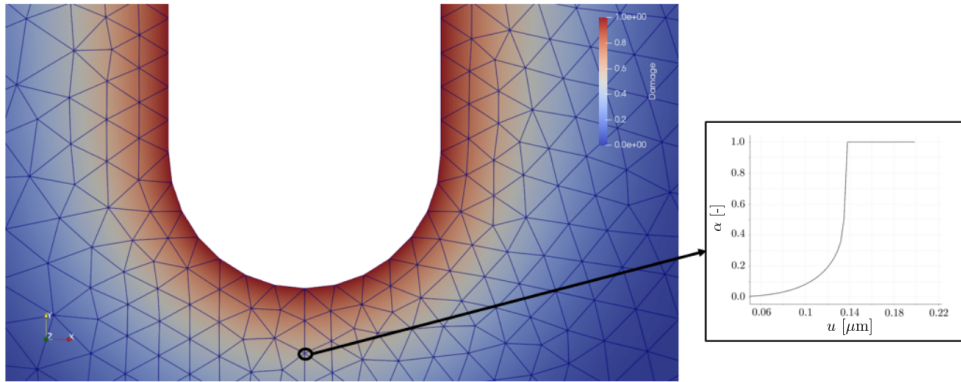


Fig. 19: Example of the damage variable. The experimental values for specimen 6 in [34] are considered ($K_c^{\text{exp}} = 1.56 \text{ MPa m}^{0.5}$ and $\sigma_c^{\text{exp}} = 2500 \text{ MPa}$).

Fig. 20 compares the three criteria. For this purpose, F_c is represented against the control parameter $l_{\text{Irwin}}/(W - a)$, keeping constant $K_c = K_c^{\text{exp}} = 1.56 \text{ MPa m}^{0.5}$ and the dimensions of the specimen, i.e., varying only σ_c . First, it is noticed that for small values of $l_{\text{Irwin}}/(W - a)$ the three criteria lead to the same estimation of F_c . An example of this situation was shown in Figs. 18 and 19, where $l_{\text{Irwin}}/(W - a) = 0.12$. On the other hand, for bigger values of $l_{\text{Irwin}}/(W - a)$ it is shown in Fig. 20 that the FU criterion provides a larger estimation of F_c than the αU and KU criteria, while the latter two always coincide. For these values, as mentioned earlier, the PF model does not predict a crack in the Griffith sense, and the failure of the structure is due to the diffusion and propagation of damage in a certain region. This means that although the stiffness decreases, the diffusion must grow even more to observe a drop in the force-displacement diagram, as shown in Fig. 21 for $l_{\text{Irwin}}/(W - a) = 0.77$, where the critical points obtained the two criteria (FU and KU) are highlighted (αU provides the same result as KU). In conclusion, for these values of l_{Irwin} so close to the specimen dimensions, these criteria may yield slightly different results, although this difference is less than 10% within the range of l_{Irwin} studied. In the results presented throughout this paper, the criterion FU is adopted, due to its similarity to the experimental procedures typically applied to analyze crack nucleation.

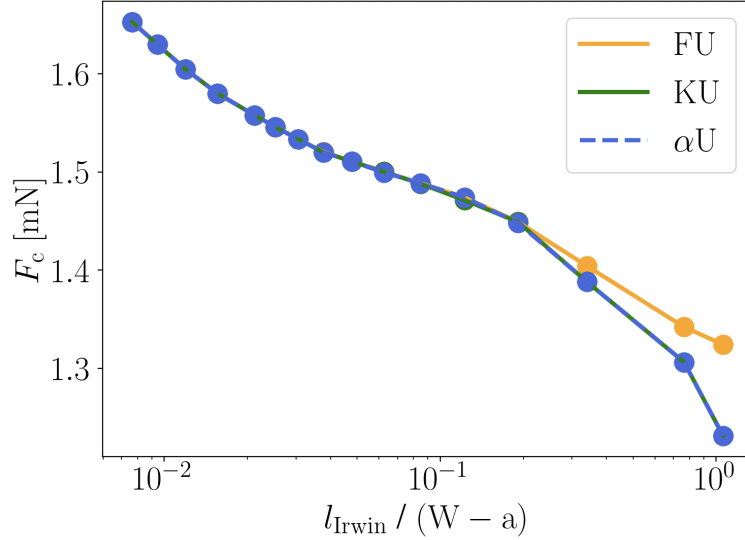


Fig. 20: Evolution of F_c as a function of l_{Irwin} for the three criteria established for crack nucleation: FU, KU and αU . The fracture toughness is constant in this analysis and equal to the experimental value measured in [34], $K_c = K_c^{\text{exp}} = 1.56 \text{ MPa m}^{0.5}$.

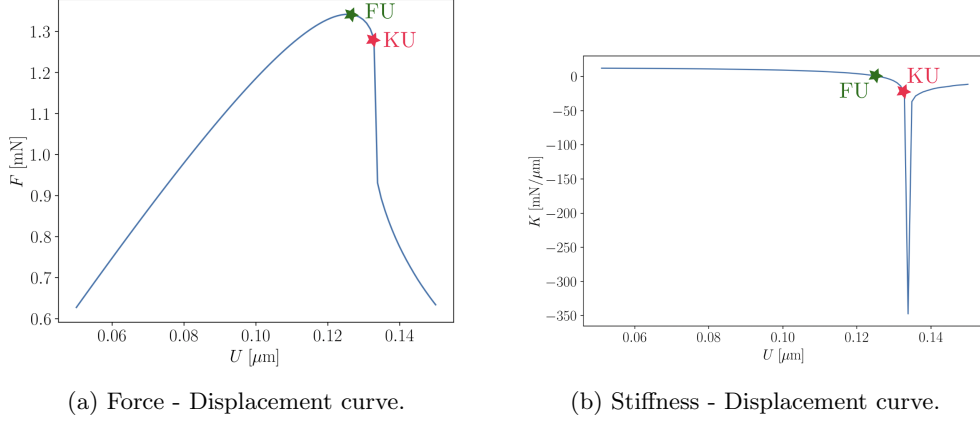


Fig. 21: Examples of a force-displacement and stiffness-displacement curve. These curves were obtained using the fracture properties and dimensions experimentally obtained in [34] for specimen 6 ($K_c^{\text{exp}} = 1.56 \text{ MPa m}^{0.5}$ and $\sigma_c^{\text{exp}} = 1000 \text{ MPa}$).

Fig. 22 compares the PF model and the CC, representing F_c with respect to the control parameter $l_{\text{Irwin}}/(W - a)$. Notice that a lower value of $l_{\text{Irwin}}/(W - a)$ corresponds to a higher value of σ_c , what is related to a greater F_c . Two options in the PF model for the damage boundary condition are used, NDBC and DBC1. It is observed that both the CC and PF model qualitatively exhibit the same trend. When l_{Irwin} is of the order of the specimen dimensions, F_c loses its dependence on σ_c (and therefore on l_{Irwin}), as it is an energy criterion that governs failure. However, when $l_{\text{Irwin}} \ll (W - a)$, a tensile criterion governs crack nucleation, and this is perceived through the strong dependence of F_c on σ_c , represented here as a strong dependence on l_{Irwin} . Similar conclusions are obtained in [13], where the control parameter is the phase field length scale divided by the size of an initial defect. In [11], this analysis is presented only for the CC at the microscale, where the specimen size is so small that the energy criterion completely governs crack nucleation (there is not energy available for the crack to be nucleated). Generally, the difference between the CC and PF model does not exceed 15%. In the region where the Irwin length is of the order of the specimen dimensions, the difference between the CC and the NDBC option is the greatest; that is, imposing the condition $\alpha = 1$ at the blunt radius approximates the results of the PF model and the CC for that range of l_{Irwin} . However, for small values of l_{Irwin} , this difference appears to be smaller in the case of NDBC. This may be because the DBC1 conditions contribute to localize the damage at the notch tip, even when the damaged region is large, as is the case for $l_{\text{Irwin}} \approx (W - a)$. In general, by imposing the DBC1 conditions, the critical load is underestimated compared to the other two approximations.

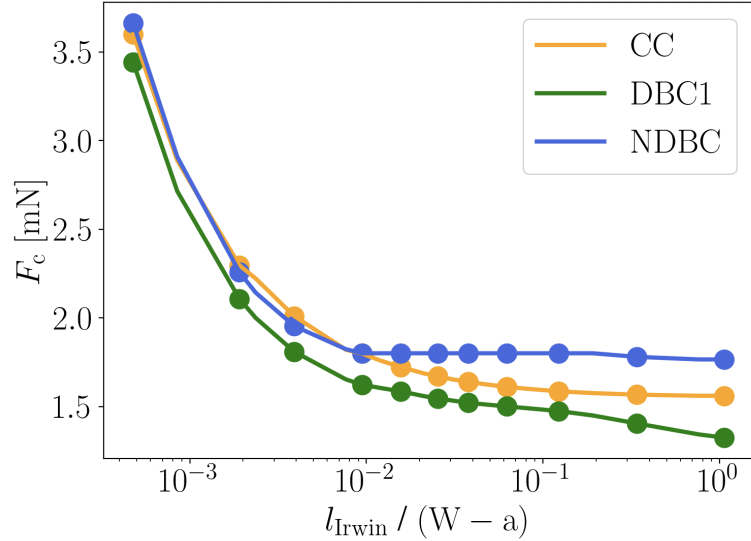


Fig. 22: Evolution of F_c as a function of $l_{\text{Irwin}}/(W - a)$ for the PF model (NDBC and DBC1) and the CC. The fracture toughness is constant in this analysis and equal to the experimental value obtained in [34], $K_c = K_c^{\text{exp}} = 1.56 \text{ MPa m}^{0.5}$.

4 Comparison to experiments

In previous sections it has been shown that both the CC and the PF model yield different results when the Irwin length and the dimensions of the specimen are similar. Therefore, a comparison to experiments is necessary to ascertain whether these models are able to describe crack nucleation at the micro-scale.

4.1 Experiments conducted by Parvizi et al.

In Section 3.1, an intriguing strengthening effect is observed for sufficiently small specimen lengths in the tensile test of a brittle, homogeneous material. However, it is crucial to acknowledge that such effects may manifest differently depending on the specific circumstances of the problem. To illustrate this variability, the experimental investigations conducted by Parvizi et al. [38] are analyzed. In their study, tensile tests were conducted to explore transverse cracking in a cross-ply laminate composed of glass fiber epoxy. Remarkably, Parvizi et al. found that the observed strengthening effect is controlled by the thickness of the transverse ply, denoted as e . This delay in crack initiation is known as in-situ effect and has been widely studied. Models at the macroscale in composite laminates can be found in [39] where an analytical procedure based on Fracture Mechanics is proposed, and in [4, 40] where Finite Fracture Mechanics is applied to study the previously mentioned experiments by Parvizi et al. [38]. A more advanced concept that studies this phenomenon at the microscale can be

found in [16], where a micromechanical analysis is made to study the in-situ effect of this problem applying the PF model.

The material properties considered in the numerical simulations used to represent the set of experiments made by Parvizi et al. are as follows: Young's modulus $E_1 = 42$ GPa, $E_2 = 14$ GPa, Poisson's ratio $\nu_{12} = 0.278$, critical energy release rate $G_{c2} = 0.12$ MPa mm, and tensile strength $\sigma_{c2} = 84$ MPa, obtained from experimental data reported in [38] and [41]. Hence, the Irwin length is $l_{\text{Irwin}} = 0.24$ mm. Notice that the model studied assumes that crack nucleation appears only in the transverse ply [38]. At this stage, it is important to emphasize that this paper focuses on nucleation rather than the propagation of cracks within the inner ply. Consequently, multiple transverse cracking is not studied, although this aspect has been successfully addressed in [16, 42, 43].

This problem can be approached analytically by applying the CC model, as described in [4]. Analysis within this framework reveals that for small values of e , the failure mechanism is governed by an energy criterion. Consequently, a structural strengthening effect is observed due to the small size of the specimen. On the other hand, the PF model can be applied on a two-dimensional (2D) equivalent model, assuming plane strain conditions, as depicted in Fig. 23. This corresponds to a cylindrical bending assumption for the laminate plate.

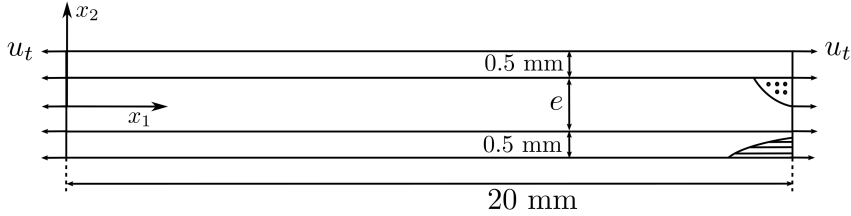


Fig. 23: Scheme of the equivalent 2D model that illustrates the experiments conducted by Parvizi et al. [38].

Although two PF models are studied, the so-called AT1 and AT2, only AT1 is ultimately represented. This decision stems from the fact the AT2 model estimates a critical strain of $\varepsilon_c = 0.9\%$ for values of the transverse ply thickness where experimental observations yield approximately $\varepsilon_c \approx 0.6\%$. As discussed in Section 3.1, the tensile test can be modeled using the PF approach, considering both homogenized and localized solutions (BC1 and BC2) [7]. Among these two models, the BC1 is represented in Fig. 24 to compare with predictions obtained using the CC and experiments, since BC2 yields the same results as BC1. Looking at Fig. 24, the critical longitudinal stress σ_{1c} is represented as a function of e/l_{Irwin} . It is important to highlight that in this paper $\sigma_{1c} = E_2\varepsilon_{1c}$ for the sake of simplicity, although a more precise calculation would include the laminate theory and would slightly differ from the one presented here [41]. Notice that in Fig. 24 the parameter used is e/l_{Irwin} instead of l_{Irwin}/e (used

in previous sections). The change has been made for the sake of analogy with the experimental representation in [38].

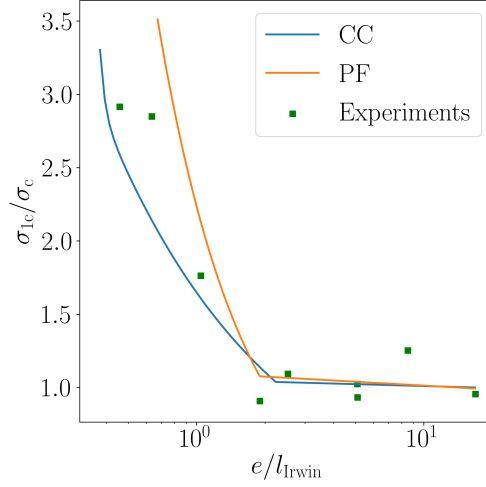


Fig. 24: Critical longitudinal stress σ_{1c} represented against the control parameter e/l_{Irwin} estimated by experiments and the numerical predictions using both the PF and the CC model.

Fig. 24 shows that the predictions obtained by the PF model and the CC are in qualitative agreement. The greatest quantitative disparity is observed when e approaches l_{Irwin} . In that case a structural strengthening effect emerges, captured by the two numerical estimations and the experimental results.

One of the critical aspects when investigating this problem using the PF model is the definition of crack nucleation, and different criteria can be applied, as studied in Section 3.3. In this case, the evolution of α is considered, i.e., the crack nucleation is located at the point where the maximum value of the damage variable in the structure α_{max} reaches 1. This criterion is chosen over parameters such as the global elastic energy Ψ_{el} or the stiffness in the specimen, since failure detection might be inadequate for very small values of the transverse layer thickness, where failure of the central ply is described by the development of an almost homogeneous damage field, instead of localized crack-like damage bands. An example of this is shown in Fig. 25 where α_{max} and Ψ_{el} are represented for a very thin transversal ply ($e = 0.2$ mm). The control parameter is in this case $e/l_{Irwin} = 0.84$.

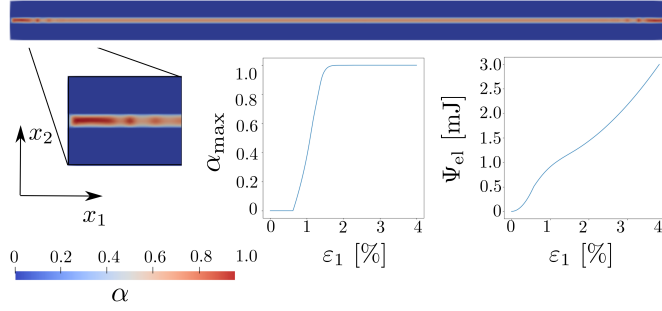


Fig. 25: Evolution of α for a thin case ($e = 0.2$ mm), considering the AT1 model and the BC2 solution. Two variables are represented with respect to ε_x [%], the maximum damage value in the structure, α_{\max} , and the elastic energy in the transverse ply Ψ_{el} .

The limitation mentioned above does not apply to larger values of e , as shown in Fig. 26 for $e = 2$ mm. In this scenario, it is observed that at the point where a decrease in the elastic energy of the transverse ply occurs, the phase field variable abruptly changes from 0 to 1 at a specific location in the structure, where the crack is nucleated. Notice that in this case the thickness is much bigger than the Irwin length, i.e., the control parameter $e/l_{Irwin} = 8.4$. The failure is described by an array of crack-like solutions with localized damage.

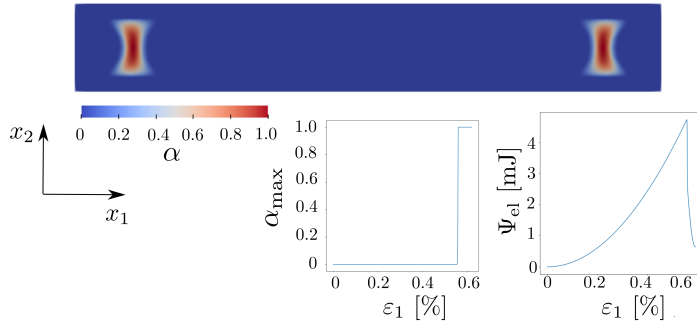


Fig. 26: Evolution of α for a thick case ($e = 2$ mm), considering the AT1 model and the BC2 solution. Two variables are represented with respect to ε_x [%], the maximum damage value in the structure, α_{\max} , and the elastic energy in the transverse ply Ψ_{el} .

4.2 Experiments conducted by Henry et al.

Bending tests of microcantilever beams offer enhanced reliability compared to, for example, tensile tests, as it incorporates the application of a notch to localize crack nucleation far away from the region of load application. This practice effectively mitigates local effects according to the Saint-Venant principle. In 2019, Henry et al. [34]

conducted experimental investigations to determine the fracture toughness of 8Y-FSZ cubic zirconia considering this technique under force and displacement control. A scheme of the experiments is shown in Fig.27, where the main dimensions used to describe the specimen are highlighted. A total of 14 specimens were tested, considering the material properties $E = 216$ GPa and $\nu = 0.22$. The tensile strength of this material was also predicted as 2.5 ± 0.7 GPa using bending tests on unnotched specimens (a total of 4 specimens were tested for that purpose).

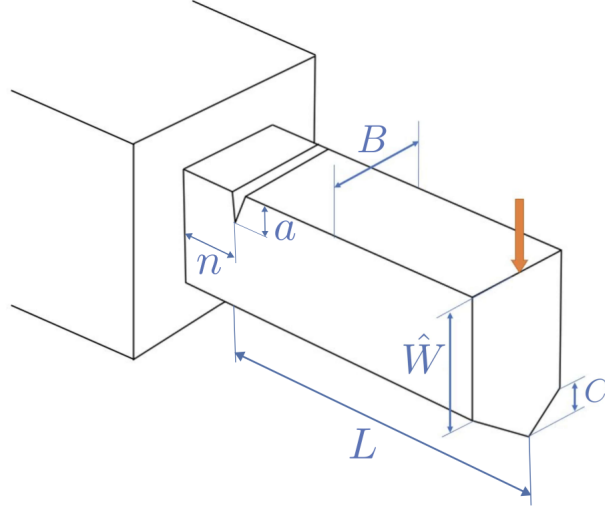


Fig. 27: Scheme of the experiments performed by Henry et al. in [34].

In Section 3.3 an equivalent 2D model (see Fig. 14) is used to represent these experiments, readjusting the height of the 2D specimen, W , to consider the pentagonal shape of the cross section in the real model highlighted in Fig. 27, so that $W = \hat{W} + C/2$. In Table 2 the main dimensions of the equivalent 2D model for each specimen are summarized, as well as the critical force and the fracture toughness experimentally obtained in [34].

Index	L [μm]	W [μm]	B [μm]	n [μm]	a [μm]	F_c^{exp} [mN]	K_c^{exp} [$\text{MPa} \cdot \text{m}^{0.5}$]
1	9.20	4.34	5.98	0.920	1.32	1.53	1.44
2	9.97	4.04	4.99	0.997	0.64	1.53	1.50
3	9.74	5.01	6.27	0.974	0.70	3.28	1.57
4	9.10	4.66	6.21	0.910	0.61	2.27	1.14
5	8.03	4.20	4.57	0.803	0.56	2.29	1.65
6*	8.76	4.26	4.42	0.876	0.91	1.51	1.56
7*	12.11	3.32	4.40	1.211	0.64	0.87	1.63
8	8.76	4.30	4.99	0.876	0.50	2.75	1.68
9	8.13	4.57	5.34	0.813	0.42	3.68	1.59
10	7.19	4.12	3.45	0.719	0.84	1.28	1.42
11	7.33	4.60	4.18	0.733	0.56	2.13	1.29
12	9.40	4.13	4.56	0.940	0.70	1.46	1.41
13	7.08	4.35	5.25	0.708	0.83	2.21	1.35
14*	9.96	3.50	3.94	0.996	0.63	0.82	1.32

Table 2: Geometrical parameters and experimental results of the 14 different specimens tested in [34]. The specimens highlighted by * were tested using displacement control, whereas the others were tested using force control.

A critical force numerically obtained F_c^{num} is calculated considering the CC and PF model to compare with experiments, assuming the mechanical properties obtained in [34]. Hence, for each specimen the fracture toughness considered is $K_c = K_c^{\text{exp}}$. In case of displacement control, F_c^{num} is obtained applying (25). Under force control, the critical distributed force applied in the structure t_c is used to calculate the critical force F_c ,

$$F_c^{\text{num}} = t_c W B. \quad (26)$$

In addition, it is important to highlight that two set of damage boundary conditions are studied for the PF model, as explained in Section 3.3: non-damaged boundary conditions (ndbc) and damaged boundary conditions at the blunt of the notch (dbc).

Fig. 28 shows the parameter $F_c^{\text{num}}/F_c^{\text{exp}}$ for each specimen. In general, the PF model with no damaged boundary conditions tends to overestimate the experimental predictions, with an average relative error of 11.2% with respect to the experimental values. Nevertheless, it appears to be a reasonable approximation for specimens 7, 8 and 9, which are underestimated by both the CC and the PF with damaged boundary conditions. In the case of the CC the average relative error with respect to experiments is 5.7%, whereas for PF dbc the average is 8.5%, suggesting they offer a better approximation than the PF ndbc. Looking at this comparison, we can conclude that both the PF model and the CC can predict experimental results.

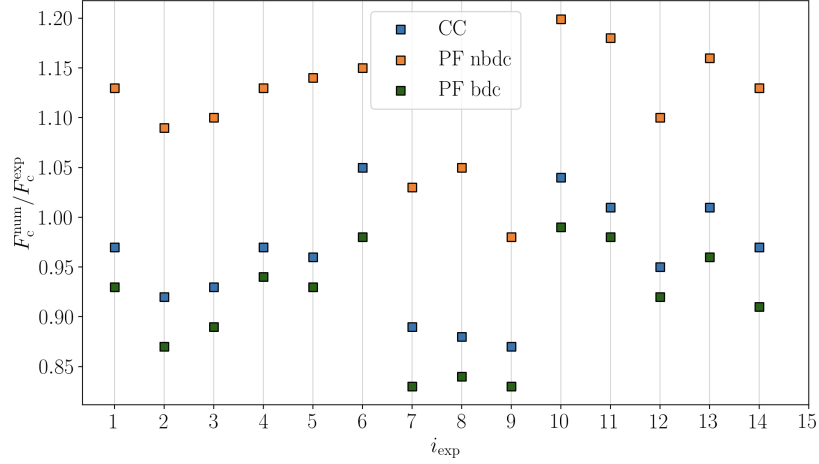


Fig. 28: A comparison between experimental results obtained in [34] and those obtained applying the PF model and the CC is presented. For the PF model, two options are investigated: one with damaged (dbc) and the other with non-damaged (nbdc) boundary conditions on the U-notch.

Furthermore, the same parameter $F_c^{\text{num}} / F_c^{\text{exp}}$ is also represented with respect to $l_{\text{Irwin}} / (W - a)$ in Fig. 29, only for the PF dbc and the CC, the two closest distributions. It is observed that the biggest difference between the CC and the PF model with damaged boundary conditions is given when $l_{\text{Irwin}} / (W - a)$ reaches the highest value (for specimen number 7 in Fig. 28), with a difference of 7%. On the contrary, the smallest difference, around 3%, is attributed to the smallest value of $l_{\text{Irwin}} / (W - a)$.

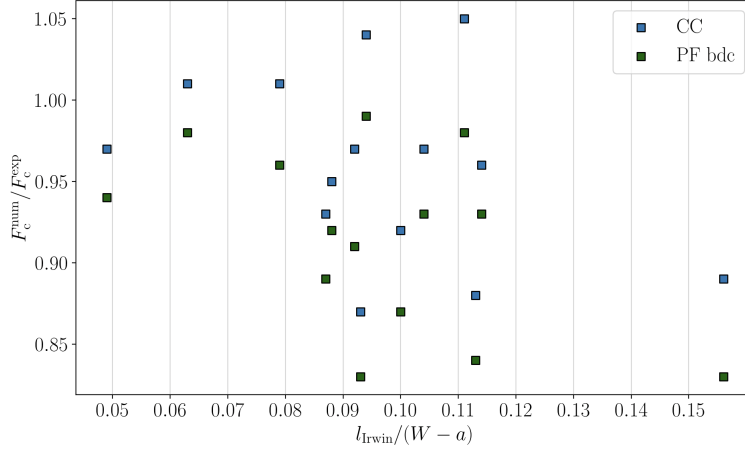


Fig. 29: Effect of $l_{Irwin}/(W - a)$ in the critical force obtained in experiments [34] and numerical simulations, considering the PF model and the CC. For the PF model, two options are investigated: one with damaged and the other with non-damaged boundary conditions on the u-notch.

5 Conclusions

This study compares the answer of both the CC and the PF model in different scenarios, changing the ratio between the Irwin length and the dimensions of the specimen, a common case observed in brittle materials when the scale of the problem is changed from the macro to the microscale. As a general conclusion, it has been shown that the two models predict different results when the Irwin length is of the order of the dimensions of the specimen, therefore interacting with the dimensions of the structure. The reason is that while the CC model consistently defines a discontinuous crack, the PF model represents a damage model where the stiffness degradation occurs within a localized region, and therefore a Griffith like crack is no longer predicted. On the contrary, when the Irwin length is much smaller than the dimensions of the specimen the same results are obtained from both the PF and the CC.

When the Irwin length is of the order of the dimensions of the specimen, the fracture behaviour of the structure can change. One of the observed changes is a structural strengthening effect, i.e., the maximum allowable stress reached in the structure is higher than the tensile strength considered in the definition of the Irwin length (an input in both the CC and the PF model). This conclusion, that might indicate that the failure stress is a structural property rather than a material characteristic in those situations, is captured by both the CC and PF model considered in this paper. However, different quantitative results are obtained and this is explained by the different mechanisms that each model is describing. In the CC, this effect is attributed to the small specimen size, leading to crack nucleation governed by the energy criterion. Conversely, the apparent strengthening effect in the PF model is more related to the size of the damage region, so significant that an increase in the load is required to reach

a complete structural failure. In other words the PF model is defining a quasi-brittle behaviour when the Irwin length is of the order of the dimensions of the specimen, whereas the CC is always describing a brittle failure.

In this paper, the critical load is used to compare the results obtained by the CC and the PF model. In the latter, three criteria are considered to define this parameter: FU, KU, and αU . The FU criterion predicts a higher critical load compared to the KU and αU criteria when the Irwin length approaches the specimen dimensions; otherwise, all three criteria yield the same results. Additionally, it is observed that the critical load has less dependency on the tensile strength when the Irwin length is of the order of the specimen dimensions. The CC explains this by suggesting that an energy criterion governs failure in such situations. This qualitative conclusion is captured by both the CC and the PF model.

Comparison with experimental data reveals that while there are differences between the two models, these disparities are not significant enough to unequivocally determine a method that clearly gives better predictions at the microscale. Both models exhibit a good agreement with experimental observations, despite their differences. Furthermore, incorporating a damaged boundary condition in the blunt of the notch when applying the PF model in the context of U-notches provides a closer approximation to experimental outcomes and aligns the results more closely with those predicted by the CC model.

To sum up, this paper addresses the differences and similarities between two of the most commonly used models for predicting fracture, the CC and the PF model, concluding that they differ in their predictions when the Irwin length is of the order of the dimensions of the specimen, since they are describing different failure mechanisms. Despite their differences, both models show a good agreement with experimental data. A further study would include studying and comparing other high-potential models, such as the Cohesive Zone Model [44], where a traction-separation law governs the nucleation of failure, could also be of great interest. Moreover, it would also be interesting to compare the results with a length scale insensitive phase-field damage model [45].

Acknowledgements. This paper is entirely dedicated to Professor Dominique Leguillon, the principal PhD supervisor of S. Jimenez-Alfaro. His passing left a significant void in the scientific community, not only due to his great passion and dedication but also his intelligence and creativity. Over these three years, he was a caring and patient mentor who conveyed his passion for science and his extensive experience as an educator. His most valuable lesson was undoubtedly learning to enjoy research despite its challenges. Dominique, your memory and teachings will always be with us. Thank you for everything.

The funding received from the European Union's Horizon 2020 research and innovation programme under Marie Skłodowska-Curie grant agreement No. 861061-NEWFRAC is gratefully acknowledged.

S. Jimenez-Alfaro also acknowledges the Iberdrola Foundation under the Marie Skłodowska-Curie Grant Agreement No 101034297.

J. Reinoso is grateful to Ministerio de Ciencia e Innovación de España through the Project TED2021-131649B-I00.

Declarations

References

- [1] Heimann, R.B.: Classic and advanced ceramics: From fundamentals to applications. *Classic and Advanced Ceramics: From Fundamentals to Applications* (2010) <https://doi.org/10.1002/9783527630172>
- [2] Schuh, C.: Nanoindentation studies of materials. *Materials today* **9**(5), 32–40 (2006) [https://doi.org/10.1016/S1369-7021\(06\)71495-X](https://doi.org/10.1016/S1369-7021(06)71495-X)
- [3] Dehm, G., Jaya, B., Raghavan, R., Kirchlechner, C.: Overview on micro- and nanomechanical testing: New insights in interface plasticity and fracture at small length scales. *Acta Materialia* **142**, 248–282 (2018) <https://doi.org/10.1016/j.actamat.2017.06.019>
- [4] Leguillon, D.: Strength or toughness? A criterion for crack onset at a notch. *European Journal of Mechanics - A/Solids* **21**(1), 61–72 (2002) [https://doi.org/10.1016/S0997-7538\(01\)01184-6](https://doi.org/10.1016/S0997-7538(01)01184-6)
- [5] Weißgraber, P., Hell, S., Becker, W.: Crack nucleation in negative geometries. *Engineering Fracture Mechanics* **168**, 93–104 (2016) <https://doi.org/10.1016/j.engfracmech.2016.02.045> . Modeling of fracture and damage in composite materials
- [6] Pham, K., Marigo, J.-J.: Approche variationnelle de l’endommagement: I. les concepts fondamentaux. *Comptes Rendus Mécanique* **338**(4), 191–198 (2010)
- [7] Pham, K., Amor, H., Marigo, J.-J., Maurini, C.: Gradient damage models and their use to approximate brittle fracture. *International Journal of Damage Mechanics* **20**(4), 618–652 (2011)
- [8] Ambati, M., Gerasimov, T., De Lorenzis, L.: Phase-field modeling of ductile fracture. *Computational Mechanics* **55**, 1017–1040 (2015)
- [9] Doitrand, A., Henry, R., Meille, S.: Brittle material strength and fracture toughness estimation from four-point bending test. *Journal of Theoretical, Computational and Applied Mechanics* (2021) <https://doi.org/10.46298/jtcam.6753>
- [10] Gallo, P., Saporà, A.: Brittle failure of nanoscale notched silicon cantilevers: a finite fracture mechanics approach. *Applied Sciences* **10**(5), 1640 (2020) <https://doi.org/10.3390/app10051640>
- [11] Jiménez-Alfaro, S., Leguillon, D.: Finite fracture mechanics at the micro-scale. application to bending tests of micro cantilever beams. *Engineering Fracture Mechanics* **258**, 108012 (2021) <https://doi.org/10.1016/j.engfracmech.2021.108012>

- [12] Baldassari, M., Monaco, A., Saporita, A., Cornetti, P.: Size effect on flexural strength of notched and un-notched concrete and rock specimens by finite fracture mechanics. *Theoretical and Applied Fracture Mechanics* **125**, 103787 (2023) <https://doi.org/10.1016/j.tafmec.2023.103787>
- [13] Tanné, E., Li, T., Bourdin, B., Marigo, J.-J., Maurini, C.: Crack nucleation in variational phase-field models of brittle fracture. *Journal of the Mechanics and Physics of Solids* **110**, 80–99 (2018) <https://doi.org/10.1016/j.jmps.2017.09.006>
- [14] Guillén-Hernández, T., García, I., Reinoso, J., Paggi, M.: A micromechanical analysis of inter-fiber failure in long reinforced composites based on the phase field approach of fracture combined with the cohesive zone model. *International Journal of Fracture* **220**, 181–203 (2019) <https://doi.org/10.1007/s10704-019-00384-8>
- [15] Fantoni, F., Bacigalupo, A., Paggi, M., Reinoso, J.: A phase field approach for damage propagation in periodic microstructured materials. *International Journal of Fracture* **223**, 53–76 (2020) <https://doi.org/10.1007/s10704-019-00400-x>
- [16] Guillén-Hernández, T., Quintana-Corominas, A., García, I., Reinoso, J., Paggi, M., Turón, A.: In-situ strength effects in long fibre reinforced composites: A micro-mechanical analysis using the phase field approach of fracture. *Theoretical and Applied Fracture Mechanics* **108**, 102621 (2020) <https://doi.org/10.1016/j.tafmec.2020.102621>
- [17] Macías, J., Arteiro, A., Otero, F., Camanho, P.P., Reinoso, J.: Micro-mechanical analysis of composite materials using phase-field models of brittle fracture. *European Journal of Mechanics-A/Solids* **102**, 105069 (2023) <https://doi.org/10.1016/j.euromechsol.2023.105069>
- [18] Awaji, H., Nishimura, Y., Choi, S.-M., Takahashi, Y., Goto, T., Hashimoto, S.: Toughening mechanism and frontal process zone size of ceramics. *Journal of the Ceramic Society of Japan* **117**(1365), 623–629 (2009)
- [19] Bažant, Z.P., Kazemi, M.T.: Size effect in fracture of ceramics and its use to determine fracture energy and effective process zone length. *Journal of the American Ceramic Society* **73**(7), 1841–1853 (1990)
- [20] Molnár, G., Doitrand, A., Estevez, R., Gravouil, A.: Toughness or strength? regularization in phase-field fracture explained by the coupled criterion. *Theoretical and applied fracture mechanics* **109**, 102736 (2020) <https://doi.org/10.1016/j.tafmec.2020.102736>
- [21] Doitrand, A., Molnár, G., Estevez, R., Gravouil, A.: Strength-based regularization length in phase field fracture. *Theoretical and Applied Fracture Mechanics* **124**, 103728 (2023)

- [22] Molnár, G., Doitrand, A., Lazarus, V.: Phase-field simulation and coupled criterion link echelon cracks to internal length in antiplane shear. *Journal of the Mechanics and Physics of Solids*, 105675 (2024) <https://doi.org/10.1016/j.jmps.2024.105675>
- [23] Griffith, A.A.: VI. The phenomena of rupture and flow in solids. *Philosophical transactions of the royal society of London. Series A, containing papers of a mathematical or physical character* **221**(582-593), 163–198 (1921) <https://doi.org/10.1098/rsta.1921.0006>
- [24] Marigo, J.-J., Maurini, C., Pham, K.: An overview of the modelling of fracture by gradient damage models. *Meccanica* **51**, 3107–3128 (2016) <https://doi.org/10.1007/s11012-016-0538-4>
- [25] Miehe, C., Welschinger, F., Hofacker, M.: Thermodynamically consistent phase-field models of fracture: Variational principles and multi-field fe implementations. *International journal for numerical methods in engineering* **83**(10), 1273–1311 (2010)
- [26] Amor, H., Marigo, J.-J., Maurini, C.: Regularized formulation of the variational brittle fracture with unilateral contact: Numerical experiments. *Journal of the Mechanics and Physics of Solids* **57**(8), 1209–1229 (2009) <https://doi.org/10.1016/j.jmps.2009.04.011>
- [27] Bourdin, B., Marigo, J.-J., Maurini, C., Sicsic, P.: Morphogenesis and propagation of complex cracks induced by thermal shocks. *Physical review letters* **112**(1), 014301 (2014)
- [28] Francfort, G.A., Marigo, J.-J.: Revisiting brittle fracture as an energy minimization problem. *Journal of the Mechanics and Physics of Solids* **46**(8), 1319–1342 (1998) [https://doi.org/10.1016/S0022-5096\(98\)00034-9](https://doi.org/10.1016/S0022-5096(98)00034-9)
- [29] Ambrosio, L., Tortorelli, V.M.: Approximation of functional depending on jumps by elliptic functional via t-convergence. *Communications on Pure and Applied Mathematics* **43**(8), 999–1036 (1990) <https://doi.org/10.1002/cpa.3160430805>
- [30] Bourdin, B., Francfort, G.A., Marigo, J.-J.: Numerical experiments in revisited brittle fracture. *Journal of the Mechanics and Physics of Solids* **48**(4), 797–826 (2000) [https://doi.org/10.1016/S0022-5096\(99\)00028-9](https://doi.org/10.1016/S0022-5096(99)00028-9)
- [31] Barrata, I.A., Dean, J.P., Dokken, J.S., HABERA, M., HALE, J., Richardson, C., Rognes, M.E., Scroggs, M.W., Sime, N., Wells, G.N.: Dolfinx: The next generation fenics problem solving environment (2023)
- [32] Hofer, A.-K., Walton, R., Ševeček, O., Messing, G.L., Bermejo, R.: Design of damage tolerant and crack-free layered ceramics with textured microstructure. *Journal of the European Ceramic Society* **40**(2), 427–435 (2020) <https://doi.org/>

- [33] Zolesi, C., Maurini, C.: Stability and crack nucleation in variational phase-field models of fracture: effects of length-scales and stress multi-axiality (2024)
- [34] Henry, R., Blay, T., Douillard, T., Descamps-Mandine, A., Zacharie-Aubrun, I., Gatt, J., Langlois, C., Meille, S.: Local fracture toughness measurements in polycrystalline cubic zirconia using micro-cantilever bending tests. *Mechanics of Materials* **136**, 103086 (2019) <https://doi.org/10.1016/j.mechmat.2019.103086>
- [35] Henry, R., Zacharie-Aubrun, I., Blay, T., Chalal, S., Gatt, J., Langlois, C., Meille, S.: Fracture properties of an irradiated PWR UO₂ fuel evaluated by micro-cantilever bending tests. *Journal of Nuclear Materials* **538**, 152209 (2020) <https://doi.org/10.1016/j.jnucmat.2020.152209>
- [36] Navidtehrani, Y., Betegón, C., Martínez-Pañeda, E.: A simple and robust abaqus implementation of the phase field fracture method. *Applications in Engineering Science* **6**, 100050 (2021) <https://doi.org/10.1016/j.apples.2021.100050>
- [37] Klinsmann, M., Rosato, D., Kamlah, M., McMeeking, R.M.: An assessment of the phase field formulation for crack growth. *Computer Methods in Applied Mechanics and Engineering* **294**, 313–330 (2015)
- [38] Parvizi, A., Garrett, K., Bailey, J.: Constrained cracking in glass fibre-reinforced epoxy cross-ply laminates. *Journal of Materials Science* **13**(1), 195–201 (1978) [https://doi.org/10.1016/0010-4361\(87\)90006-1](https://doi.org/10.1016/0010-4361(87)90006-1)
- [39] Camanho, P.P., Dávila, C.G., Pinho, S.T., Iannucci, L., Robinson, P.: Prediction of in situ strengths and matrix cracking in composites under transverse tension and in-plane shear. *Composites Part A: Applied Science and Manufacturing* **37**(2), 165–176 (2006) <https://doi.org/10.1016/j.compositesa.2005.04.023>
- [40] García, I., Mantič, V., Graciani, E.: Debonding at the fibre–matrix interface under remote transverse tension. one debond or two symmetric debonds? *European Journal of Mechanics-A/Solids* **53**, 75–88 (2015) <https://doi.org/10.1016/j.euromechsol.2015.02.007>
- [41] García, I., Mantič, V., Blázquez, A., París, F.: Transverse crack onset and growth in cross-ply [0/90] s laminates under tension. application of a coupled stress and energy criterion. *International journal of Solids and Structures* **51**(23-24), 3844–3856 (2014) <https://doi.org/10.1016/j.ijsolstr.2014.06.015>
- [42] Jalalvand, M., Hosseini-Toudeshky, H., Mohammadi, B.: Numerical modeling of diffuse transverse cracks and induced delamination using cohesive elements. *Proceedings of the Institution of Mechanical Engineers, Part C: Journal of Mechanical Engineering Science* **227**(7), 1392–1405 (2013)

- [43] Karoui, Z., Berthe, J., Maurini, C.: Non-uniform spacing of transverse cracks in symmetric composite laminates. *International Journal of Fracture* **242**(2), 191–206 (2023) <https://doi.org/10.1007/s10704-023-00715-w>
- [44] Barenblatt, G.I.: The mathematical theory of equilibrium cracks in brittle fracture. *Advances in applied mechanics* **7**, 55–129 (1962)
- [45] Wu, J.-Y., Nguyen, V.P.: A length scale insensitive phase-field damage model for brittle fracture. *Journal of the Mechanics and Physics of Solids* **119**, 20–42 (2018) <https://doi.org/10.1016/j.jmps.2018.06.006>